Journal of Solid State Chemistry **160,** 435–443 (2001)
doi:10.1006/jssc.2001.9271, available online at http://www.idealibrary.com on IDEAL®

Pillaring of Layered Perovskites, $K_{1-x}La_xCa_{2-x}Nb_3O_{10}$, with Nanosized Fe_2O_3 Particles

Yang-Su Han,* Shin-Hei Choi,* Jae-Up Jang,† and Dong-Kuk Kim*,[1]

*Department of Chemistry, College of Natural Sciences, Kyungpook National University, Taegu 702-701, Korea; and †School of Chemistry, Seoul National University, Seoul 151-742, Korea

Received February 16, 2001; in revised form May 24, 2001; accepted June 8, 2001

Nanosized Fe_2O_3 clusters are pillared in the interlayer spaces of layered perovskites, $H_{1-x}La_xCa_{2-x}Nb_3O_{10}$ ($0 \le x \le 0.75$) by a guest-exchange reaction using the trinuclear acetato-hydroxo iron cation, $[Fe_3(OCOCH_3)_7\ OH \cdot 2H_2O]^+$. The interlayer spaces of niobate layers are pre-expanded with *n*-butylammonium cations (n-$C_4H_9NH_3^+$), which are subsequently replaced by bulky iron pillaring species to form Fe(III) complex intercalated layer niobates. Upon heating at 380°C, the interlayered acetato-hydroxo iron complexes are converted into Fe_2O_3 nanoclusters with a thickness of *ca.* 3.5 Å irrespective of the interlayer charge density (x). The band-gap energy of the Fe_2O_3 pillars ($E_g \sim 2.25$ eV) is slightly larger than that of bulk Fe_2O_3 ($E_g \sim 2.20$ eV) but is smaller than that expected for such a small-sized semiconductor, which can be assigned to the pancake-shaped Fe_2O_3 pillars of 3.5 Å in height with comparatively large lateral dimension. X-ray absorption spectroscopic measurements at the Fe *K*-edge are carried out in order to obtain structural information on the Fe_2O_3 pillars stabilized between the niobate layers. XANES analysis reveals that the interlayer FeO_6 octahedra have coordination environments similar to that of bulk α-Fe_2O_3, but noncentrosymmetric distortion of interlayered FeO_6 is enhanced due to the asymmetric electric potential exerted by the negatively charged niobate layers. Scanning electron microscopic observation and nitrogen adsorption–desorption isotherm measurement suggest that the pillared derivatives are nanoporous materials with the highest BET specific surface area of *ca.* 116 m²/g. © 2001 Academic Press

Key Words: **layered perovskite; XANES; pillaring; nanoporous; layer charge.**

INTRODUCTION

Layered metal oxides such as layered titanates and niobates including $K_2Ti_4O_9$, $KTiNbO_5$, $K_4Nb_6O_{17}$, $KCa_2Nb_3O_{10}$, *etc.*, are of special interest because of their unique intercalation behavior and possible applications to conversion of solar energy into chemical energy as well as detoxification of hazardous organics (1–6). Since these layered titanates and niobates are typical semiconductive oxides, they can produce photoelectrons and holes under band-gap irradiation ($E_g = 3.2$–3.5 eV), thus acting as promising UV photocatalysts. From a structural viewpoint, they consist of two-dimensional MO_6 ($M = Ti^{4+}$ and Nb^{5+}) octahedral layers and exchangeable alkali metal cations (usually K^+) that compensate for the negative charges of the layers.

$KCa_2Nb_3O_{10}$ is a typical example of a layered perovskite with the Dion–Jacobson phase (7) that can be represented by the general formula of $M[A_{n-1}B_nO_{3n+1}]$, where $M = K^+$, Rb^+, $A = Ca^{2+}$, Pb^{2+}, La^{3+}, and $B = Nb^{5+}$, Ta^{5+}, Ti^{4+}, *etc.* and $n = 2$ or 3. The interlayered alkali metal cations in this type of material are readily exchanged with various organic and inorganic species to form intercalative layer nanohybrids (8–12). Pillaring of layered metal oxides with inorganic oxide clusters is another promising way to prepare nanoporous layer hybrids (3, 5, 13–20) with large nanoporosity, specific surface area, and intrinsic catalytic activity.

From the viewpoint of photocatalysts, pillaring of semiconductor nanoparticles with small band-gap energy between the perovskite-type niobate layers is of special interest. Besides the enhanced nanoporosity and specific surface areas, the integration of a small band-gap semiconductor with a large band-gap one (niobate layer) on a nanometer scale order offers an opportunity to sensitize the latter, thus allowing the utilization of visible light. Furthermore, the coupling of different semiconductors with different energy levels is also very useful in achieving efficient charge separation by heterogeneous charge transfer (21), which improves the energy conversion efficiency and photocatalytic activity.

In the present study, we describe a pillaring of semiconductive Fe_2O_3 nanoclusters in the interlayer space of a perovskite-type layered metal oxide to construct porous layer nanocomposites. A trinuclear acetato-hydroxo iron(III) nitrate, $[Fe_3(OCOCH_3)_7OH \cdot 2H_2O]NO_3$, and $K_{1-x}La_x$

[1]To whom correspondence should be addressed. Fax: +82-53-950-5331. E-mail: kimdk@knu.ac.kr.

0022-4596/01 $35.00
Copyright © 2001 by Academic Press
All rights of reproduction in any form reserved.

$Ca_{2-x}Nb_3O_{10}$ ($0 \leq x \leq 0.75$) with variable interlayer charge densities were used as a pillar precursor and host matrix, respectively. The effect of interlayer charge density (x) on the pillaring reaction, interlayer pillar structure, and porous texture is investigated thoroughly. In addition, the electronic structure and local coordination environment of the interlayered Fe_2O_3 nanoclusters are also studied using Fe *K*-edge X-ray absorption spectroscopy and diffuse reflectance UV spectroscopy.

EXPERIMENTAL

1. Preparation of Fe_2O_3-Pillared Layered Perovskites

A series of $K_{1-x}La_xCa_{2-x}Nb_3O_{10}$ ($x = 0.00$, 0.25, 0.50, and 0.75) was prepared by reacting appropriate quantities of K_2CO_3, La_2O_3, $CaCO_3$, and Nb_2O_5 at 1000°C–1200°C for 48 h with one grinding in between. Excess (10 mol%) K_2CO_3 was added to compensate for the loss due to volatilization. Thus, prepared K-forms were converted into proton (H^+) derivatives by refluxing the solids in 4 N HCl at room temperature for 24 h under continuous stirring. The interlayer protons were replaced again by *n*-butylammonium ($C_4H_9NH_3^+$) molecules in order to expand the gallery height and to facilitate the subsequent pillaring reaction of bulky Fe cluster cations. The alkylammonium intercalation reaction was carried out at room temperature by an acid–base reaction. Typically, 1 g of proton derivative was reacted with butylamine (5 ml) in ethanol solution (10 ml) for 24 h. The reaction products were separated by centrifugation, washed with distilled water several times, and then dried in a vacuum.

A trinuclear acetato-hydroxo iron(III) nitrate, $[Fe_3(OCOCH_3)_7OH \cdot 2H_2O]NO_3$, was prepared according to the method reported previously (22). The procedure was partly modified as follows: $Fe(NO_3)_3 \cdot 9H_2O$ (40.4 g) was added to 25 ml of ethyl alcohol and then 70 ml of acetic anhydride was reacted by addition in small portions. When the reaction started with evolution of heat, the reactant was cooled in an ice bath. After all the acetic anhydride parts were reacted, the solution was cooled using ice and the resulting precipitate was separated by filtration and used as pillar precursor without washing.

A Fe_2O_3 pillar was constructed in the interlayer space of $H_{1-x}La_xCa_{2-x}Nb_3O_{10}$, preswelled with butylammonium molecules using iron acetato-hydroxo cation. In a typical reaction, butylammonium derivative was reacted with $[Fe_3(OCOCH_3)_7OH \cdot 2H_2O]^+$ at 60°C for 48 h in aqueous solution. The molar ratio of $[Fe_3(OCOCH_3)_7OH \cdot 2H_2O]^+/(C_4H_9NH_3^+)_xLa_xCa_{2-x}Nb_3O_{10}$ was adjusted to 30. The obtained sample, after being centrifuged and washed with water, was dried in a vacuum. Finally, the interlayer iron acetato-hydroxo complex was converted into a Fe_2O_3 cluster by calcining at 380°C and 500°C for 4 h under an ambient atmosphere.

2. Characterization

The crystalline phases of the products were identified with a power X-ray diffractometer (MacScience MXP-3) using Ni-filtered Cu$K\alpha$ radiation ($\lambda = 1.5405$ Å). The specimens for XRD measurements were prepared by spreading wet samples on slide glasses to make a preferred orientation. Thermal analysis for the Fe-acetato-hydroxo complex intercalated layer perovskite was performed on a Seiko TG/DTA320 instrument under an ambient atmosphere. Diffuse reflectance spectra of the powders were measured using a Varian Cary 5G UV–vis–NIR spectrophotometer. The band-gap energy (E_g) of the pillared products was determined from the onset of reflection spectra calculated according to the following equation (23),

$$\alpha h\nu = A(h\nu - E_g)^n,$$

where α is the reflection coefficient, $h\nu$ is the photon energy, and n is the constant, depending on the type of semiconductor ($n = 1/2$ and 2 for direct interband transition and indirect interband transition, respectively). Nitrogen adsorption–desorption isotherms of the pillared samples were measured volumetrically at liquid nitrogen temperature with a Sorptomatic 1990 (CE Instruments) equipped with a computer-controlled measurement system. All the samples were degassed at 250°C for 5 h under reduced pressure (< 1 torr) prior to sorption measurements. Specific surface areas were estimated using both BET and Langmuir equations. The micropore surface area (S_{micro}) and external surface area ($S_{external}$) were also calculated on the basis of the *t*-plot method of nitrogen (24). Field emission scanning electron microscopy (FE-SEM) was carried out with a Hitachi S-4200 electron microscope, operating at 30 kV. Specimens for observation under an electron microscope were prepared by dispersing finely ground pillared samples in ethanolic solution by ultrasonication for 10 min, drying, and coating with Pt–Rh for 180 sec in a vacuum.

X-ray absorption spectra (XAS) at the Fe *K*-edge were recorded at the Pohang Accelerator Laboratory (PAL) on beamline BL3C1 operating at 2.5 GeV with *ca.* 100–150 mA of stored current. The radiation was monochromatized using a Si(311) double crystal monochromator to collect high-resolution XAS spectra. Data were collected in a transmission mode with N_2 gas-filled ionization chambers as detectors. The absorption energy was calibrated by simultaneously measuring an Fe metal foil standard, assigning the first inflection point to 7111.2 eV (25). The XANES spectral analyses were processed according to the following procedure using the program WinXAS: the spectra were normalized in absorbance by fitting the spectral region from 7090 to 7110 eV (the region before the pre-edge) using a first-order polynomial function and subtracting this as background absorption. Thereafter, the edge jump was

normalized to a value of 1 for the absorption, based on the linear variation of the average absorption coefficient of the spectral region from 7200 to 7250 eV.

RESULTS AND DISCUSSION

1. X-Ray Diffraction Analysis

Powder X-ray diffraction patterns of the pristine $KCa_2Nb_3O_{10}$ and its proton derivative were successfully indexed on the basis of tetragonal unit cells with $a = 3.864$ Å, $c/2 = 14.633$ Å and $a = 3.851$ Å, $c = 14.793$ Å, respectively, which shows good agreement with those values of previous report (8). The reduced charged compounds of $K_{1-x}La_xCa_{2-x}Nb_3O_{10}$ also formed a single phase isostructural with the parent $KCa_2Nb_3O_{10}$ over the composition range ($0.25 \leq x \leq 0.75$). The intercalation compound between the $HCa_2Nb_3O_{10}$ and *n*-butylamine exhibited a basal spacing of 25.5 Å, corresponding that the *n*-butylammonium cations form bilayer arrangements between the inorganic slabs with a tilting angle of $\sim 56^\circ$, which is well consistent with the value reported by Jacobson *et al.* (10). Even with a low density of interlayer protons, facile intercalation of butylamines occurs in the series of $H_{1-x}La_xCa_{2-x}Nb_3O_{10}$, with nearly the same lattice expansion (~ 25 Å) as with the parent compound $HCa_2Nb_3O_{10}$. This intercalation behavior of $H_{1-x}La_xCa_{2-x}Nb_3O_{10}$ is comparable to that of $Ag_6Mo_{10}O_{33}$ (26, 27), where even with a low packing density of amines (area/chain > 50 Å^2), gauche block structures are stabilized.

2. Thermal Analysis

Thermogravimetric (TG) and differential thermal analysis (DTA) curves of the Fe-acetato-hydroxo complex intercalated $Ca_2Nb_3O_{10}$ sample ($x = 0.00$) are plotted in Fig. 1. The first step weight loss accompanied by an endothermic peak around 150°C can be attributed to the dehydration of the interlayer water, or in part, the dehydroxylation of partially hydrolyzed iron hydroxides. The drastic weight loss in the temperature range of 250–350°C with an intense exothermic reaction corresponds to the oxidative decomposition of acetyl groups of the interlayer complex ions. Comparing decomposition of the acetyl group occurring at 235–250°C in pure acetato-hydroxo iron complex (28), it is likely that the partial bonding to the negatively charged niobate layers would result in the thermal decomposition of the complex at a higher temperature. The acetyl/Fe(III) ratio calculated from the weight loss in the complex intercalated samples was found to be less than that in the pure complex (acetyl/Fe = 6/3 in mole), suggesting that the trinuclear acetate complex ions are taken up by niobate layers in partly hydrolyzed forms (28, 29). An additional exothermic reaction occurs around 380°C together with a small weight loss in TG, which can be ascribed to the

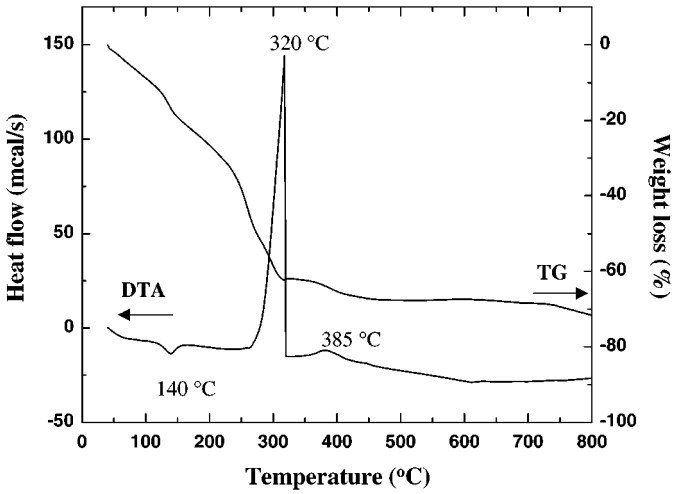

FIG. 1. Thermogravimetric (TG) and differential thermal analysis (DTA) curves of the $[Fe_3(OCOCH_3)_7OH \cdot 2H_2O]^+$-intercalated $Ca_2Nb_3O_{10}$.

decomposition of intermediate organic residues formed during pyrolysis. It can be expected from the TG analysis that the interlayered iron acetato-hydroxo complex would convert into iron oxide species around 380°C.

3. Pillaring Reaction

The butylammonium-intercalated layered niobates are used as precursors for the pillaring with the acetato-hydroxo iron cation, $[Fe_3(OCOCH_3)_7OH \cdot 2H_2O]^+$. The pre-expanded niobate layers facilitate the migration of bulky inorganic cations toward the interlayer ion exchange sites. Figure 2A shows the evolution of XRD patterns for the layered perovskite ($x = 0.00$) reacted with the cationic Fe complex depending upon the treatment condition. The sample dried at room temperature shows three orders of reflections corresponding to a basal spacing of 19.3 Å (a). Assuming a perovskite layer thickness of 11.5 Å (8), the gallery height is estimated to be 7.8 Å. In the pillaring of the same iron complex into aluminosilicate layers, montmorillonite (29, 30), the gallery height for the air-dried sample exhibited a value of ~ 12 Å. Thus, the observed gallery heights in the pillaring of layered perovskite are significantly smaller than in the case of layered aluminosilicates. This discrepancy may be attributed to the differences in the reaction temperatures and also in part to the nature of the inorganic layers. Yamanaka *et al.* performed the exchange reaction at 35°C (29, 30), whereas our reaction was carried out at 60°C to facilitate the incorporation of iron pillaring species into poorly swellable niobate layers. Since the trinuclear acetate iron complex ions are easily hydrolyzed in water, they have more condensed forms at the elevated reaction temperatures. Although it is not clear what kinds of

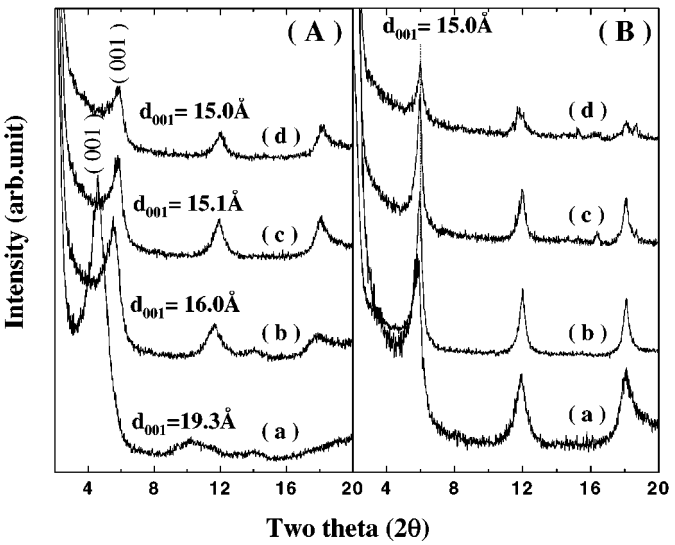

FIG. 2. Powder X-ray diffraction patterns. (A) Evolution of the XRD patterns for the $[Fe_3(OCOCH_3)_7OH\cdot 2H_2O^+]$-intercalated $Ca_2Nb_3O_{10}$ ($x = 0.00$): (a) dried in air, (b) dried at 80°C for 12 h, and (c) heat treated at 380°C and (d) 500°C for 4 h, respectively. (B) Evolution of the XRD patterns for the Fe_2O_3-pillared $La_xCa_{2-x}Nb_3O_{10}$ obtained after calcining at 380°C for 4 h: (a) $x = 0.00$, (b) $x = 0.25$, (c) $x = 0.50$, and (d) $x = 0.75$, respectively.

polymeric species are involved in the exchange reactions, it is reasonable to consider that the trinuclear acetate complex ions are taken up by perovskite layers in partly hydrolyzed forms. In addition to the hydrolysis tendency of the trinuclear acetate complex, the unique layer characteristic of the layered perovskite such as higher interlayer charge density, solid acidity, and rigidity of the perovskite slabs would also influence the interlayer structure of the guest species.

Upon drying at 80°C in air (b), the basal spacing is further decreased to 16.0 Å, which might be due to the dehydration of the interlayer water and also due to the further hydrolysis of the interlayered trinuclear acetate iron complex ions even during the drying process. When the intercalated samples are thermally treated at 380°C (c), the basal spacing is slightly decreased to 15.1 Å, yet remains almost constant up to 500°C (d). This suggests that iron oxide pillars are thermally stable at least up to 500°C. Here, the small discrepancy in the basal spacing between the sample dried at 80°C and the ones calcined at higher temperatures again supports that the intercalated organo-iron clusters are already hydrolyzed largely during the pillaring and drying processes to form more condensed iron species. The gallery heights in the calcined samples are *ca.* 3.5 Å after subtracting the thickness of the perovskite slabs, suggesting that the interlayer Fe_2O_3 may exist mainly in the form of a monolayer between niobate layers.

Figure 2B corresponds to the XRD patterns of Fe_2O_3-pillared niobates prepared by calcining at 380°C for 4 h as a function of interlayer charge density (x). The gallery heights due to the incorporation of iron oxide clusters between perovskite slabs are quite constant (*ca.* 3.5 Å), irrespective of the interlayer charge density (x). This finding suggests that the Fe_2O_3 particles constructed in the layer perovskites have the same height even though the lateral dimension is different depending upon the interlayer charge density.

4. *Diffuse Reflectance UV–Vis Spectroscopy*

The diffuse reflectance spectra of the bulk Fe_2O_3, the $[Fe_3(OCOCH_3)_7OH\cdot 2H_2O]\cdot NO_3$ precursor, and the iron species intercalated into layered niobates ($x = 0.00$) are compared in Fig. 3A after translating into the absorption mode. The inset shows the corresponding normalized absorption spectra to avoid a concentration effect. Comparing

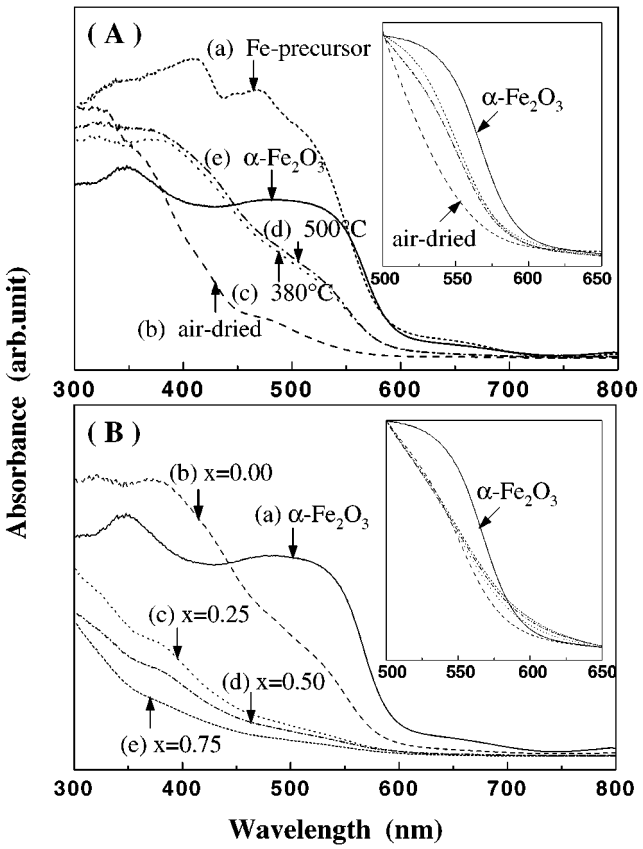

FIG. 3. UV–vis absorption spectra. (A) UV–vis absorption spectra of the (a) $[Fe_3(OCOCH_3)_7OH\cdot 2H_2O^+]NO_3$ precursor and $[Fe_3(OCOCH_3)_7OH\cdot 2H_2O^+]$-intercalated $Ca_2Nb_3O_{10}$ ($x = 0.00$), (b) dried in air, (c) heat treated at 380°C and (d) 500°C for 4 h, and (e) reference α-Fe_2O_3, respectively. (B) UV–vis absorption spectra of (a) reference α-Fe_2O_3 and the Fe_2O_3-pillared $La_xCa_{2-x}Nb_3O_{10}$ obtained after calcining at 380°C for 4 h: (b) $x = 0.00$, (c) $x = 0.25$, (d) $x = 0.50$, and (e) $x = 0.75$, respectively. The insets denote the normalized absorption spectra ($\lambda_{max} = 500$ nm).

the absorption spectra of the precursor iron complex (a) with the intercalated one, it can be found that the intercalated iron species (b) is significantly different from its precursor. As discussed above, this suggests that the partially hydrolyzed iron species are stabilized between the niobate layers. Upon heating above 380°C, the interlayered iron species are converted into Fe_2O_3 (c and d). The absorption spectra of the Fe_2O_3 immobilized in the interlayer spaces of niobates exhibit a slight spectral blue shift compared with that of bulk α-Fe_2O_3 (e) due to the size quantization effect. The band-gap energy of interlayered Fe_2O_3 is determined to be $E_g \sim 2.25$ eV, which is slightly larger than that of bulk Fe_2O_3 ($E_g = 2.19$ eV). Assuming that the pillar height of *ca.* 3.5 Å is an average dimension of the interlayered Fe_2O_3 particles, the observed band-gap energy is much smaller than that expected for such a small-sized semiconductor *via* the quantum size effect (31). Similar results were reported for iron oxide-pillared montmorillonite (32, 33), layered titanates (34), and titanium oxide-pillared montmorillonite (35), although the reason has not been yet clarified. Recently, it has been reported that the iron oxide pillars constructed in montmorillonite are in fact a pancake shape of 0.3 nm in height with a diameter of < 10 nm (36, 37). The large diameter of the semiconductor pillars is likely to contribute to the retention of the small band-gap energy.

The variation of UV absorption spectra for the Fe_2O_3-pillared samples calcined at 380°C is shown in Fig. 3B as a function of the interlayer charge density (x). The absorption intensity due to iron oxide in the range of 500–600 nm decreases with x, reflecting that the amount of incorporated Fe_2O_3 decreases as the interlayer charge density is lowered by the partial substitution Ca^{2+} for La^{3+}. Even though the difference in the absorption intensity is relatively large due to the difference in the Fe_2O_3 loading level, the band-gap energy of the pillared samples shows no significant difference as shown in the normalized absorption spectra (inset). Therefore, it can be said that the interlayered Fe_2O_3 clusters have a pancake or island shape with a thickness of 3.5 Å and comparatively large diameter.

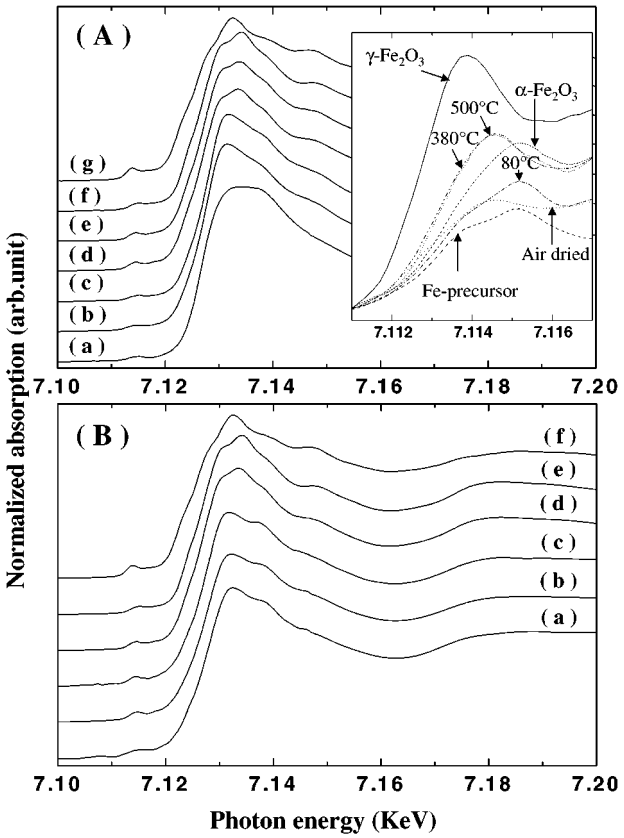

FIG. 4. Fe K-edge XANES spectra. (A) XANES spectra of the (a) $[Fe_3(OCOCH_3)_7OH\cdot 2H_2O^+]NO_3$ precursor and $[Fe_3(OCOCH_3)_7OH\cdot 2H_2O^+]$-intercalated $Ca_2Nb_3O_{10}$ ($x = 0.00$): (b) dried in air, (c) dried at 80°C for 12 h, (d) heat treated at 380°C and (e) 500°C for 4 h, and reference (f) α-Fe_2O_3 and (g) γ-Fe_2O_3, respectively. The insets denote the enlarged view of pre-edge region. (B) XANES spectra of the Fe_2O_3-pillared $La_xCa_{2-x}Nb_3O_{10}$ obtained after calcining at 380°C for 4 h: (a) $x = 0.75$, (b) $x = 0.50$, (c) $x = 0.25$, and (d) $x = 0.00$, respectively, and reference (e) α-Fe_2O_3 and (f) γ-Fe_2O_3.

5. *Fe K-Edge X-Ray Absorption Near-Edge Spectroscopy*

X-ray absorption spectroscopic measurements at the Fe K-edge were carried out in order to probe the electronic and local coordination structures of the iron oxide stabilized between niobate layers. Figure 4A shows the Fe K-edge XANES spectra for the precursor Fe complex (a) and the pillared derivatives using $HCa_2Nb_3O_{10}$ ($x = 0.00$) host (b–e) along with the reference compounds, α-Fe_2O_3 (f) and γ-Fe_2O_3 (g). An expanded view of the $1s \rightarrow 3d$ pre-edge region is shown as an inset in Fig. 4A. The XANES feature of the Fe(III)-acetato-hydroxo complex exhibits weak pre-edge peaks at 7113.8 and 7115.2 eV. Since Fe^{3+} in the $[Fe_3(OCOCH_3)_7OH\cdot 2H_2O]^+$ has a centrosymmetric octahedral site (O_h) (29), the $1s \rightarrow 3d$ transition is an electric dipole forbidden by parity consideration. Thus, the only intensity mechanism available for the $1s \rightarrow 3d$ pre-edge feature is the allowed electric quadruple transition (38–40). The observed peak splitting of *ca.* 1.4 eV in the pre-edge region of the Fe-acetato complex (inset) is also well consistent with the literature value for the high-spin ferric (d^5) complex with a centrosymmetric octahedral site (41).

When the Fe(III) acetato-hydroxo complex is intercalated into the interlayer spaces of niobate layers, the local environment around the Fe ion seems to be largely modified as evidenced by the evolution of an absorption spectrum in the entire absorption region (b). However, the edge position and the weak absorption intensity in the pre-edge region support that the Fe(III) ions still remain in octahedral sites. Thus, it is likely that the partially hydrolyzed Fe species are immobilized between the niobate layers. Upon drying the

intercalated compound at 80°C (c), the overall absorption feature is similar to that of the air-dried one. However, the pre-edge position and shape are quite similar to those of the reference α-Fe_2O_3 (f). Since the interlayer Fe-acetato-hydroxo complexes can continue hydrolysis even in the interlayer spaces during the drying process, more condensed iron hydroxide ($Fe(OH)_3$) or oxyhydroxide (FeO(OH)) species can be formed.

Upon heating of the intercalated derivatives at 380°C (d) and 500°C (e), the interlayered iron intermediate oxyhydroxide species are converted into Fe_2O_3-like ones. Comparing the overall absorption features between the calcined samples (d, e) and the reference ones (f, g), the interlayered iron oxide has electronic and crystal structures similar to those of α-Fe_2O_3 rather than γ-Fe_2O_3. A closer look into the pre-edge feature (inset), however, reveals that a stronger intensity and a lower energy shift of pre-edge peaks are observed in pillared products. Because the $1s \rightarrow 3d$ pre-edge feature is very sensitive to the geometry of the iron site, a noncentrosymmetric distortion would allow for $3d$–$4p$ mixing, thereby increasing the intensity of the pre-edge feature. The thickness of the interlayered iron oxide clusters is determined to be *ca.* 3.5 Å from the XRD analysis (Fig. 2). Thus, the interlayer FeO_6 octahedra may exist mainly in the form of a monolayer between niobate layers. The asymmetric electric potential exerted by the negatively charged niobate layers induces a noncentrosymmetric distortion of the FeO_6 octahedral layers, resulting in the enhanced pre-edge absorption. Under this circumstance, a partial electron transfer from the negatively charged niobate layers ($La_xCa_{2-x}Nb_3O_{10}^{(1-x)-}$) to the interlayer Fe_2O_3 pillars would be expected, causing the partial reduction of ferric ion. In turn, this would lead to a shift of the pre-edge absorption peak to a lower energy side for the interlayered Fe_2O_3 compared with the bulk α-Fe_2O_3.

Figure 4B compares the XANES spectra for the pillared samples thermally treated at 380°C as a function of interlayer charge density (x). As can be seen from the figure, the absorption feature for the low charged samples ($x \geq 0.25$, a–c) is distinguished from that of the pristine $HCa_2Nb_3O_{10}$ ($x = 0.00$, d). In particular, the post-edge features of the reduced charged samples are somewhat different from those of the reference and the nonreduced sample. The small pre-edge feature and the absorption peak position, however, exclude the presence of the metastable phases such as Fe_3O_4 or γ-Fe_2O_3. This indicates that the reduction of the interlayer charge density (x) by partial substitution of Ca^{2+} for La^{3+} in the $K_xLa_xCa_{2-x}Nb_3O_{10}$ decreases the iron oxide content in the interlayer spaces. Since the height of interlayer iron oxide clusters is comparatively constant (*ca.* 3.5 Å), the reduced interlayer iron oxide content would be mainly limited to the lateral dimension of pancake shaped iron oxide clusters, which subsequently modifies the interlayer pillar structure.

6. *Scanning Electron Microscopy*

The scanning electron micrographs for the pristine $HCa_2Nb_3O_{10}$ (a) and the pillared derivatives (c, d) calcined at 380°C for 4 h are represented in Fig. 5. The protonated calcium niobate (a) has plate-like morphology addressed by its crystallographic direction. All the pillared derivatives exhibit an expanded layer stacking in the interlayer direction. Among them, the highest charged sample ($x = 0.00$, b) shows a layer separation relatively larger than the others. The intercalation of *n*-butylamine molecules and pillaring of iron oxides in the interlayer spaces lead to the expansion of basal spacing, thus inducing lattice deformation. This results in the microscopic disintegration of plate-like oxide layers.

7. *Nitrogen Adsorption–Desorption Isotherm*

In order to investigate the textural evolution of the layered niobates after the pillaring reaction, nitrogen adsorption–desorption isotherms were measured at liquid nitrogen temperature. The typical N_2 isotherms of the pillared samples calcined at 380°C for 4 h are plotted in Fig. 6. In addition, the porous parameters derived from the N_2 isotherms and corresponding *t*-plots are summarized in Table 1. Upon the pillaring of the layer niobates with iron oxide clusters, the BET specific surface area largely increases compared with that of the pristine. In particular, the surface area of the unreduced charged compound ($x = 0.00$, a) reaches the value *ca.* 116 m^2/g. Although the surface area decreases with the calcination temperature, the large surface area of *ca.* 100 m^2/g is still retained even after calcination at 500°C (Table 1). This indicates that the porous structure is stable at least up to this temperature. It is worthy to note here that the adsorption isotherms fit better with the BET equation than the Langmuir one, implying that the nitrogen adsorption occurs at open surfaces where multilayer N_2 adsorption is possible. In addition, the enhanced surface area of the pillared samples mainly originates from external surfaces (mesopore or macropore) (Table 1) instead of micropore. These findings, therefore, suggest that porosity is mainly created by a turbostratic disorder structures of plate-like perovskite particles that are accompanied by intercalation and pillaring reactions. Although the pillaring of iron oxide particles causes interlayer separation (*ca.* 3.5 Å) and consequently may create many micropores between the perovskite layers, thus formed micropores are too small to be accessible to the adsorbate N_2 molecules (kinetic diameter of 7 Å). Furthermore, the pancake-shaped Fe_2O_3 nanoclusters would stuff the interlayer region (15), removing the free spaces between the niobate layers. As can be seen from Fig. 6 and Table 1, the total porosity (V_{total}) and BET specific surface area (S_{BET}) both decrease with the lowering of interlayer charge density (x). It is likely that a higher interlayer charge density is favorable to induce the

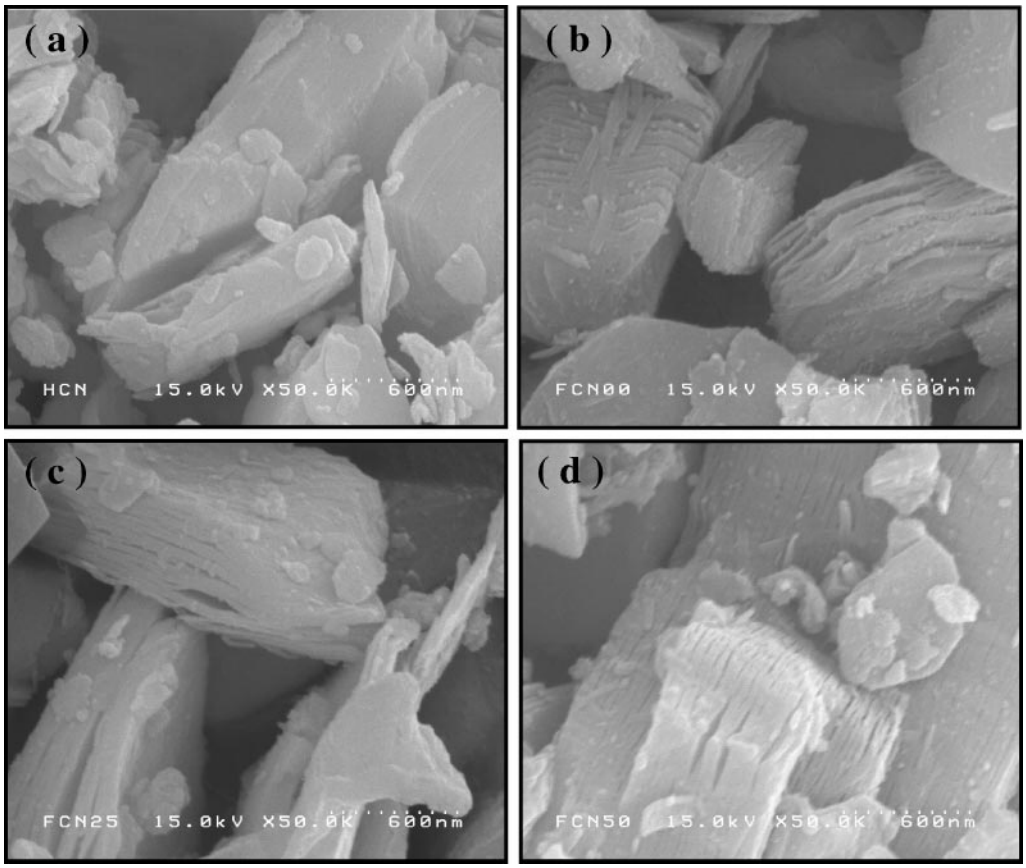

FIG. 5. Scanning electron micrographs. (a) Pristine $HCa_2Nb_3O_{10}$ and Fe_2O_3-pillared $La_xCa_{2-x}Nb_3O_{10}$ obtained after calcining at 380°C for 4 h: (b) $x = 0.00$, (c) $x = 0.25$, (d) $x = 0.50$, respectively.

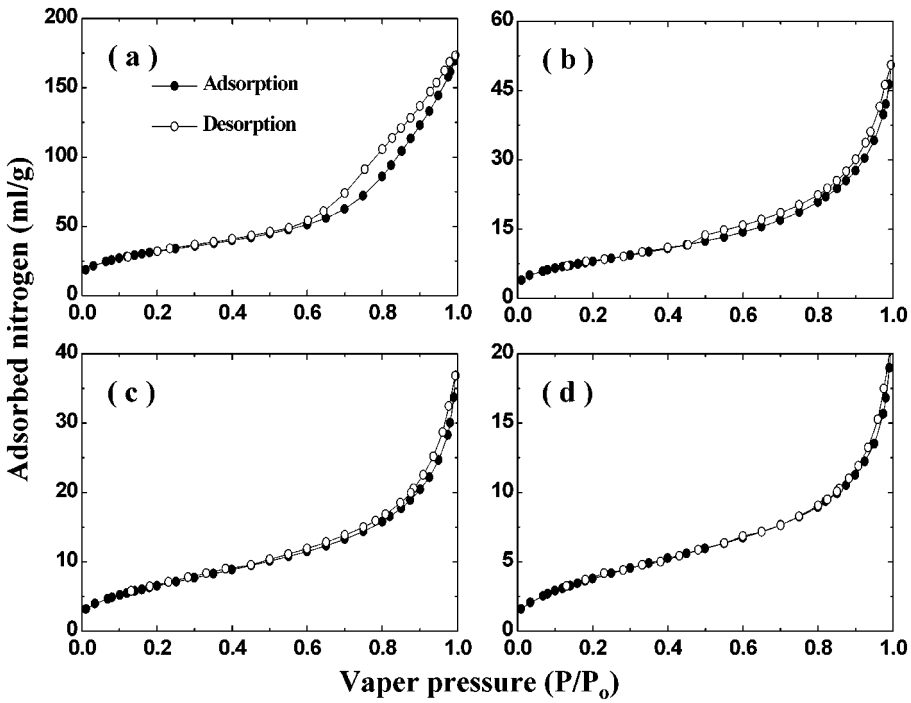

FIG. 6. Nitrogen adsorption–desorption isotherms for the Fe_2O_3-pillared $La_xCa_{2-x}Nb_3O_{10}$ samples obtained after calcining at 380°C for 4 h: (a) $x = 0.00$, (b) $x = 0.25$, (c) $x = 0.50$, and (d) $x = 0.75$, respectively.

TABLE 1
Porous Parameters of the Pristine $HCa_2Nb_3O_{10}$ and Its Pillared Derivatives

Sample		Surface area (m^2/g)				
Calcination	Interlayer charge density (x)[a]	S_{BET}	$S_{Lang.}$	S^{b}_{micro}[b]	$S_{external}$[b]	Pore volume (ml/g), V_{total}
$HCa_2Nb_3O_{10}$ (380°C/4 h)	—	2.2 (0.9999)	3.8 (0.9978)	—	2.2	7.8
380°C/4 h	0.00	115.8 (0.9999)	161.4 (0.9991)	9.2	106.6	173.3
	0.25	49.8 (0.9999)	64.5 (0.9982)	3.1	45.7	70.5
	0.50	24.9 (0.9997)	36.0 (0.9979)	—	24.9	36.8
	0.75	14.9 (0.9998)	22.2 (0.9969)	—	14.9	20.7
500°C/4 h	0.00	99.7 (0.9999)	140.1 (0.9988)	2.3	97.4	160.7
	0.25	37.0 (0.9999)	52.6 (0.9984)	—	37.0	57.7
	0.50	16.6 (0.9996)	25.9 (0.9958)	—	16.6	30.1
	0.75	9.9 (0.9998)	14.4 (0.9969)	—	9.9	16.8

[a]Interlayer charge density, $K_{1-x}La_xCa_{2-x}Nb_3O_{10}$. [b]Estimated by t-plot method. ( ) denotes the correlation factor.

turbostratic disorder structures of plate-like perovskite particles during the intercalation and pillaring reaction.

CONCLUSION

Nanosized Fe_2O_3 clusters are pillared in the interlayer spaces of layer perovskites, $H_{1-x}La_xCa_{2-x}Nb_3O_{10}$ ($0 \le x \le 0.75$), by a guest-exchange reaction using trinuclear acetato-hydroxo iron cation, $[Fe_3(OCOCH_3)_7OH \cdot 2H_2O]^+$, as iron precursor. It is proposed that the interlayer iron oxide pillars have pancake-shaped particles with substantially large lateral dimension. Fe *K*-edge XANES spectra reveal that the interlayer Fe_2O_3 nanocluster has a coordination environment similar to that of bulk α-Fe_2O_3 but experiences a noncentrosymmetric distortion due to the asymmetric electric potential exerted by the negatively charged niobate layers. Scanning electron microscopic observation and nitrogen adsorption–desorption isotherm measurement suggest that the pillared derivatives are nanoporous materials with the highest BET specific surface area of *ca.* 116 m^2/g, mainly created by the disintegration of lamellar perovskite particles during the intercalation and pillaring reaction.

ACKNOWLEDGMENTS

This work was supported by the Korea Research Foundation (KRF) (Grant No. 1998-001-D00580). Y.-S.H. and S.-H.C. thank the Ministry of Education for support through the BK21 program.

REFERENCES

1. M. Ogawa and K. Kuroda, *Chem. Rev.* **95,** 399 (1995).
2. T. Takata, A. Tanaka, M. Hara, J. N. Kondo, and K. Domen, *Catal. Today* **44,** 17 (1998).
3. R. Abe, K. Shinohara, A. Tanaka, M. Hara, J. N. Kondo, and K. Domen, *Chem. Mater.* **9,** 2179 (1997).
4. S. Ikeda, M. Hara, J. N. Kondo, K. Domen, H. Takahashi, T. Okubo, and M. Kakihana, *Chem. Mater.* **10,** 72 (1998).
5. S. Uchida, Y. Yamamoto, Y. Fujishiro, A. Watanabe, O. Ito, and T. Sato, *J. Chem. Soc., Faraday Trans.* **93,** 3229 (1997).
6. S. Ogura, M. Kohno, K. Sato, and Y. Inoue, *Phys. Chem. Chem. Phys.* **1,** 179 (1999).
7. M. Dion, M. Ganne, and M. Tournoux, *Mater. Res. Bull.* **16,** 1429 (1981).
8. A. J. Jacobson, J. T. Lewandowski, and J. W. Johnson, *J. Less-Common* Metals **116,** 137 (1986).
9. A. J. Jacobson, J. W. Johnson, and J. T. Lewandowski, *Inorg. Chem.* **24,** 3729 (1985).
10. A. J. Jacobson, J. W. Johnson, and J. T. Lewandowski, *Mater. Res. Bull.* **22,** 45 (1987).
11. R. A. Mohan Ram and A. Clearfield, *J. Solid State Chem.* **94,** 45 (1991).
12. S. Uma and J. Golpalakrishnan, *J. Solid State Chem.* **102,** 332 (1993).
13. S. Cheng and T. C. Wang, *Inorg. Chem.* **28,** 1283 (1989).
14. M. W. Anderson and J. Klinowski, *Inorg. Chem.* **29,** 3260 (1990).
15. S. Hardin, D. Hay, M. Millikan, J. V. Sanders, and T. W. Turney, *Chem. Mater.* **3,** 977 (1991).
16. M. E. Landis, B. A. Aufdembrink, P. Chu, I. D. Johnson, G. W. Kirker, and M. K. Rubin, *J. Am. Chem. Soc.* **113,** 3189 (1991).
17. R. A. Mohan Ram and A. Clearfield, *J. Solid State Chem.* **112,** 288 (1994).
18. Y. Ebina, A. Tanaka, J. N. Kondo, and K. Domen, *Chem. Mater.* **8,** 2534 (1996).

19. M. Yanagisawa, S. Uchida, Y. Fujishiro, and T. Sato, *J. Mater. Chem.* **8,** 2835 (1998).
20. F. Kooli, T. Sasaki, and M. Watanabe, *Langmuir* **15,** 1090 (1999).
21. K. R. Gopidas, M. Bohrqyez, and P. V. Kamat, *J. Phys. Chem.* **94,** 6435 (1990).
22. K. Starke, *J. Inorg. Nucl. Chem.* **13,** 254 (1960).
23. J. I. DiCosimo and C. R. Apesteguia, *J. Catal.* **116,** 81 (1989).
24. S. J. Gregg and K. S. W. Sing, "Adsorption, Surface Area and Porosity", 2nd ed. Academic Press, London, 1982.
25. R. A. Scott, J. E. Hahn, S. Doniach, H. C. Freeman, and K. O. Hodgson, *J. Am. Chem. Soc.* **104,** 5364 (1982).
26. G. Lagaly, *Solid State Ionics* **22,** 43 (1986).
27. C. Rösner and G. Lagaly, *J. Solid State Chem.* **53,** 92 (1984).
28. K. M. Parida, T. Mishra, D. Das, and S. N. Chintalpudi, *Appl. Clay Sci.* **15,** 463 (1999).
29. S. Yamanaka and M. Hattori, *Catal. Today* **2,** 261 (1988).
30. S. Yamanaka, T. Doi, and S. Sako, *Mater. Res. Bull.* **19,** 161 (1984).
31. L. Brus. *J. Chem. Phys.* **80,** 4403 (1984).
32. H. Yoneyama, S. Haga, and S. Yamanaka, *J. Phys. Chem.* **93,** 4833 (1989).
33. T. Sato, H. Okuyama, T. Endo, and M. Shimada, *React. Solids* **8,** 63 (1990).
34. Y. Fujishiro, S. Uchida, and T. Sata, *Int. J. Inorg. Mater.* **1,** 67 (1999).
35. H. Miyoshi, H. Mori, and H. Yoneyama, *Langmuir* **7,** 503 (1991).
36. T. Bakas, A. Moukarika, V. Papaefthyymiou, and A. Ladavos, *Clays Clay Minerals* **42,** 634 (1994).
37. H. Mori, H. Miyoshi, K. Takeda, H. Yoneyama, and H. Fujita, *J. Mater. Sci.* **27,** 3179 (1992).
38. R. G. Shulman, Y. Yafet, P. Eisenberger, and W. E. Blumberg, *Proc. Natl. Acad. Sci. U.S.A.* **73,** 1384 (1976).
39. C. Brouder, *J. Phys. Condens. Matter.* **2,** 701 (1990).
40. J. Wong, F. W. Lytle, R. P. Messmer, and D. H. Maylotte, *Phys. Rev. B* **30,** 5596 (1984).
41. T. E. Westre, P. Kennepohl, J. G. DeWitt, B. Hedman, K. O. Hodgson, and E. I. Solomon, *J. Am. Chem. Soc.* **119,** 6297 (1997).